Catalysis Today xxx (xxxx) xxx

Contents lists available at ScienceDirect

Catalysis Today

journal homepage: www.elsevier.com/locate/cattod

Iron-copper oxide nanoparticles supported on reduced graphene oxide for the degradation of cyclophosphamide by photo-Fenton reaction

L.T. Pérez-Poyatos [a], L.M. Pastrana-Martínez [a], S. Morales-Torres [a], P. Sánchez-Moreno [b], M. Bramini [c], F.J. Maldonado-Hódar [a,*]

[a] NanoTech – Nanomaterials and Sustainable Chemical Technologies, Department of Inorganic Chemistry, University of Granada, Granada 18071, Spain
[b] Departamento de Fisica Aplicada, Universidad de Granada, Granada 18071, Spain
[c] Departamento de Biologia Celular, Universidad de Granada, Granada 18071, Spain

ARTICLE INFO

Keywords:
Bimetallic catalysts
Cyclophosphamide
PhotoFenton
Heterogeneous catalysis
Reduced graphene oxide

ABSTRACT

Bimetallic (Fe-Cu) and reduced graphene oxide (rGO)/FeCu catalysts at 0.2% wt. were developed by a co-precipitation method, modifying the Fe-Cu molar proportions (i.e., $Fe_{40}Cu_{60}$, $Fe_{20}Cu_{80}$ and $Fe_{10}Cu_{90}$) and tested for the degradation of the cytostatic drug, cyclophosphamide (CP) in aqueous solution using the photo-Fenton process (UV-Vis). Physicochemical characterization was carried out by complementary techniques (gas adsorption, SEM, TEM, XRD, XPS) and results were correlated with the catalytic performance. The effect of pH on the degradation of the contaminant and the catalyst stability (metal leaching) were studied. The results point out the synergetic effect of the rGO/FeCu catalysts in comparison to the monometallic catalysts or without carbonaceous material. The best performance was achieved with the rGO/$Fe_{10}Cu_{90}$ catalyst achieving 82% of CP degradation at natural pH regarding 87% obtained under acid conditions (pH 3). This fact avoids the usual acidification of the solutions during Fenton-like processes and prevent the metal leaching, increasing the stability of catalysts, as demonstrated after consecutive degradation cycles, maintaining efficiency above 75%. Cytotoxicity tests certificated the low toxicity of the by-product derived from the photo-Fenton process.

1. Introduction

In the last decades, the reduction of water reserves has become a severe problem. This is partly due to their overexploitation and their contamination with different substances over the years [1]. Among these pollutants, emerging contaminants (ECs), such as pharmaceuticals and agricultural products, have experienced a large growth. Most of them are not legally regulated, even though they pose a great threat to the environment and human health, even at low concentrations (ranging between ppm and ppb) [2,3]. That exposure could cause various types of disorders in the long run, such as reproductive or neurological ones [1,4]. In particular, antineoplastic compounds used in chemotherapy are considered as hazardous, due to their mutagenic, teratogenic, genotoxic and embryotoxic potential [4,5]. In general, these substances are extremely soluble in water, which makes their transport in this medium especially easy. Nevertheless, there is a lack of research regarding antineoplastic degradation also influenced by their low concentrations in the environment compared to other pharmaceuticals (i.e., paracetamol, ibuprofen, amoxicillin, among others) more generally consumed [5,6]. Among these, cyclophosphamide (CP) is one of the most cytotoxic drugs used in Europe for the treatment of breast and ovarian cancers, and in recent studies, it has been confirmed that around 20% of the drug is excreted without being metabolized [7,8].

Frequently, the treatments used in conventional water treatment plants are not enough to degrade ECs, due to their high persistence and toxicity [9,10]. For this purpose, advanced oxidation processes (AOPs) are increasingly being used for the treatment of sewage waters [11,12]. These are based on the in situ generation of radicals with a high oxidation potential, namely the hydroxyl radicals, $OH^{\bullet}$ (with an oxidation potential of 2.8 eV). The Fenton process is one of the most efficient for this purpose. It is based on the reaction between Fe^{2+} and H_2O_2 for the generation of hydroxyl radicals, responsible of mineralizing these organic compounds to H_2O and CO_2 [9,13]. Among the advantages of this process, low cost, efficient degradations for a large number of organic compounds and reaction conditions at room temperature and atmospheric pressure notably stand out [13–15]. However, the

* Corresponding author.
E-mail address: fjmaldon@ugr.es (F.J. Maldonado-Hódar).

https://doi.org/10.1016/j.cattod.2023.01.017
Received 29 October 2022; Received in revised form 15 December 2022; Accepted 22 January 2023
Available online 23 January 2023

homogeneous Fenton process presents some disadvantages associated to the recuperation and reuse of catalysts, catalyst deactivation due to Fe^{3+} precipitation or a great dependence on pH [13,14]. Moreover, this process needs an additional step in the water treatment process, because of the presence of metals in solution and consequently, they must be precipitated before the treated water is casted into the environment [15, 16].

The development and use of heterogeneous Fenton-like catalysts is the alternative to overpass these difficulties maintaining the commented advantages [15]. Although iron is the most common transition metal used in Fenton-like processes, other metals, such as copper, nickel, cobalt, molybdenum, and so on are promising alternatives [17,18]. In particular, Cu-catalysts show low cost and toxicity (the legal limit is 2 mg/L for Cu, regarding 0.2 mg/L for Fe) [19], larger pH range of operation (even reaching neutral and alkaline values) and smaller deactivation of copper ions by formation of complexes with organic byproducts [15,16,20]. Bimetallic catalysts based on iron and copper present the advantage of synergistic effect between them, enhancing activity regarding monometallic catalysts, based on Eqs. 1–6.

$$Cu^{2+} + H_2O_2 \rightarrow Cu^{+} + HOO^{\bullet} + H^{+} \quad (1)$$

$$Cu^{+} + H_2O_2 \rightarrow Cu^{2+} + OH^{-} + OH^{\bullet} \quad (2)$$

$$Fe^{3+} + Cu^{+} \rightarrow Fe^{2+} + Cu^{2+} \quad (3)$$

$$Fe^{2+} + H_2O_2 \rightarrow Fe^{3+} + HO^{-} + HO^{\cdot} \quad (4)$$

$$Fe^{2+} + HO^{\bullet} \rightarrow Fe^{3+} + HO^{-} \quad (5)$$

$$Fe^{3+} + H_2O_2 \rightarrow Fe^{2+} + H^{+} + HO_2^{\bullet} \quad (6)$$

The slow Fe^{3+} reduction in monometallic catalysts is accelerated by the electron transfer in the bimetallic ones, forming also Cu^{+} species able to react with H_2O_2 in a similar way than Fe^{2+} to generate additional $OH^{\bullet}$ radicals and Cu^{2+}, with the advantage that Cu^{2+} reduction is faster than in the case of Fe^{3+} ions (Eq. 2) [20,21]. Additional synergetic effects are developed by using carbon supports because their great superficial area is key to achieving high adsorption of the contaminant over the catalyst [22,23]. Additionally, carbon material can avoid to a greater extent nanoparticle aggregation and leaching, helping with catalyst stability. Moreover, due to their electronic properties, carbons also play an important role in enhancing electron transfer redox reactions with the metallic active phase (semiconductor) [15]. In previous studies, mostly Fe or Cu monometallic catalysts, or Fe-Cu mixed ferrites were used for the degradation of CP with the photoFenton process. Emídio et al. [24] achieved a degradation of around 70% of a solution of 7.7 μmol/L of CP, in approximately 150 min at near-neutral pH values with a mixed Fe-Cu ferrite. Lutterbeck et al. [25] reached 90% degradation of a 20 ppm CP solution in 250 min, at pH 5, using $FeSO_4$ as homogeneous catalyst. The development of bimetallic catalysts supported on carbon materials can be useful to achieve a better degradation of the pollutant in a shorter time, due to a synergic effect between both metals, and at wider pH ranges and avoiding metal leaching to a larger extent.

In this work, various catalysts were synthesized, based on Fe and Cu oxides with different molar proportions ($Fe_{40}Cu_{60}$, $Fe_{20}Cu_{80}$ and $Fe_{10}Cu_{90}$) and supported on rGO with a loading of 0.2% wt. These catalysts were evaluated on the degradation of the cytostatic compound cyclophosphamide (CP). To the best of our knowledge, this is one of the limited works focused on the degradation of antineoplastic compounds, such as CP, using the photoFenton process with bimetallic catalysts supported on graphene derivatives. The role of each component and the best experimental conditions were determined.

2. Materials and methods

2.1. Chemicals

Iron (II) acetate ($Fe(OAc)_2$, 95%, Aldrich); copper (II) acetate ($Cu(OAc)_2{\cdot}H_2O$, Probus); graphite oxide (previously synthesized by Hummers method); distilled water; Milli-Q water; sodium borohydride ($NaBH_4$, >98%, Sigma Aldrich); ethylene glycol (>99%, Labkem); sodium sulfite (Na_2SO_3, 98%, Carlo Erba Reagents); hydrochloric acid (HCl, 37%, Labkem); hydrogen peroxide (H_2O_2, 30%, VWR Chemicals); cyclophosphamide, CP ($C_7H_{15}Cl_2N_2O_2P{\cdot}H_2O$, >98%, TCI); titanium oxysulfate (IV) ($TiOSO_4$, Merck), sulphuric acid (H_2SO_4, 95%, VWR Chemicals); sodium hydroxide (NaOH, Fluka Chemika); iron (II) sulphate ($FeSO_4{\cdot}7\,H_2O$, VWR Chemicals); copper (II) sulphate ($CuSO_4{\cdot}5\,H_2O$, Panreac).

2.2. Synthesis of bimetallic Fe_xCu_y – oxide catalysts and rGO/ bimetallic Fe_xCu_y catalysts

Bimetallic Fe_xCu_y – oxide catalysts were prepared using aqueous solutions of iron and copper acetates, i.e., $Fe(OAc)_2$ and $Cu(OAc)_2$ as metal precursors, where their proportions were fitted according to their molecular weight, to obtain $Fe_{10}Cu_{90}$, $Fe_{20}Cu_{80}$ and $Fe_{40}Cu_{60}$ catalysts. As an example, for rGO/$Fe_{10}Cu_{90}$ sample, 0.0164 g of $Fe(OAc)_2$ and 0.141 g of $Cu(OAc)_2{\cdot}H_2O$ were used, while for the unsupported $Fe_{10}Cu_{90}$ sample were utilized 0.124 and 1.116 g of $Fe(OAc)_2$ and $Cu(OAc)_2{\cdot}H_2O$, respectively. Then, a $NaBH_4$ solution containing 10-fold molar ratio is added and homogenized by stirring at room temperature. The mixture is left to react for 2 h and the solids filtered with a cellulose membrane, washed with abundant Milli-Q water, dried overnight at 100 ℃and finally, finely grinded [26].

The procedure of the rGO/bimetallic Fe_xCu_y catalysts implies the preparation of two solutions, the first one containing the fitted amounts of acetate precursors, as previously described. On the other hand, graphite oxide was suspended in 200 mL of ethylene glycol (EG) and the mixture is sonicated for several hours to achieve complete exfoliation of graphite oxide to graphene oxide (GO). Graphite oxide was previously synthesized by a modified Hummers method as described elsewhere [27]. Then, the solution of salts with the appropriate proportion is added to the GO suspension and the mixture is left at reflux during 5 h at 85 ℃ using an oil bath. Ethylene glycol could act as a reducing agent, obtaining a partial reduction of GO by chemical treatment (mainly associated to the reduction of epoxy groups in GO), developing partially reduced graphene oxide (rGO) [28]. After cooling at room temperature, solids are separated from EG by centrifugation (5000 rpm for 20 min) and washed with acetone and water. Solids are maintained within the minimum volume of water (~50–70 mL) and this suspension is freezed for later freeze-drying to finally obtain the catalysts [26]. Freeze-drying is useful to control nanoparticle distribution on rGO [29]. The catalysts containing a total metal loading of 0.2% wt. on rGO are named as: rGO/$Fe_{10}Cu_{90}$, rGO/$Fe_{20}Cu_{80}$ and rGO/$Fe_{40}Cu_{60}$. For comparison purposes, rGO/Fe and rGO/Cu catalysts, both with a metal loading of 0.2% wt., were also synthesized following the same procedure described previously.

2.3. Characterization techniques

Catalysts were characterized by applying different complementary techniques. Thermogravimetric analysis (TGA) and differential scanning calorimetry (DSC) were carried out using a thermogravimetric analyzer Mettler Toledo, model TGA-DSC1. The morphology of the catalysts was studied by scanning electronic microscopy (SEM), with a Carl Zeiss SMT, model Auriga, high resolution microscope. Transmission electronic microscopy (TEM) images were taken using a Thermo Fischer Scientific Talos F200X high resolution transmission electronic microscope. X-ray diffraction (XRD) patterns were obtained with a Bruker D8 Discover

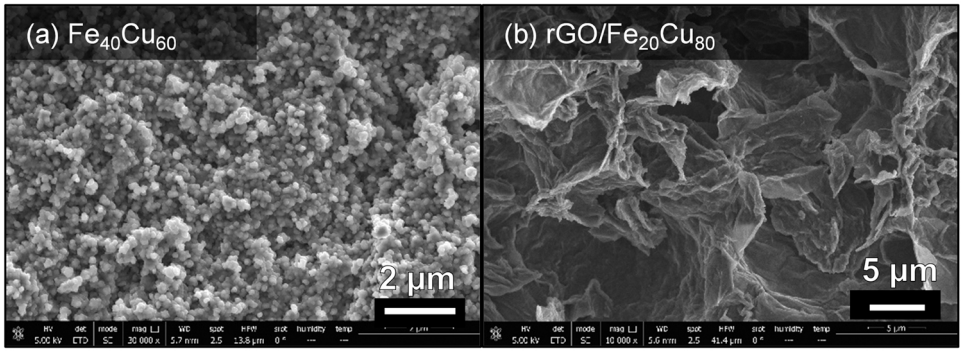

Fig. 1. SEM images for a) $Fe_{40}Cu_{60}$ and b) rGO/$Fe_{20}Cu_{80}$ catalysts.

diffractometer. The average crystal size (D_p) of the materials was calculated by applying the Scherrer equation [30]. The surface chemistry of samples was characterized by X-ray photoelectron spectroscopy (XPS) using a Physical Electronic spectrometer (PHI 5701 system) equipped with a Mg 1253.6 eV standard source at 300.0 W and hemispherical electron analyzer.

N_2 physical adsorption at − 196 ℃ was also used to obtain the adsorption-desorption isotherms. These were recorded using a Quadrasorb SI equipment from Quantachrome. Previously, the samples were outgassed by being subjected to high vacuum (10^{-6} mbar) at 110 ℃ for 12 h. Surface area S_{BET} for the catalysts was calculated with the Brunauer, Emmett and Teller method (BET) [31]; and the pore size distribution and medium pore diameter (D_p), with the Barrett, Joyner and Halenda (BJH) method applied to N_2 desorption branch [32]. Total pore volume (V_T) is considered as adsorbed N_2 volume at relative pressures (P/P_0) of 0.95, while mesopore volume (V_{meso}) is calculated using Gurvich rule, as the difference between V_T and adsorbed N_2 volume at P/P_0 of 0.4.

The point of zero charge (pH_{pzc}) was obtained with the following method [33]. A 1:10 ratio between catalyst and water is maintained, respectively (in this case, 50 mg of catalyst and 5 mL of Milli-Q water). This water was previously degassed to remove CO_2 present in it and avoid its acidic influence. The suspensions were shaken periodically in the next few days and its pH was measured until it reached a constant value, which was considered the pH_{pzc}.

2.4. Degradation study of CP with photoFenton process

All the synthesized catalysts were evaluated on the degradation of the antineoplastic compound CP, using batch reactors and 100 mL of a 20 mg/L (7.6×10^{-5} mol L^{-1}) aqueous solution of the pollutant, a catalyst load of 0.5 g/L and near UV-Vis radiation, at room temperature (25 ℃). The experiments were performed at natural pH (around 6.0). Moreover, experiments at acidic and basic pH were carried out by adding HCl or NaOH solutions, respectively. Then, the solution was magnetically stirred under dark conditions for 1 h and purged with air flow to establish the adsorption-desorption equilibrium. The adsorption capacity was around 6% and 15% of the initial CP concentration for Fe_xCu_y and rGO/ bimetallic Fe_xCu_y catalysts, respectively. Once the dark phase concludes, photodegradation experiments are carried out, the stoichiometric concentration of H_2O_2 (2 mM) is added and simultaneously, the lamp is turned on (C_0). For this purpose, a medium pressure vapor mercury lamp was used, with near UV-Vis radiation ($\lambda > 365$ nm), 125 Wm^{-2} of power, and maintaining constant stirring and O_2 flow. The amount of irradiance entering the photoreactor was around to 25–30 mW cm^{-2}. The reactor is supplied with a cooling jacket to maintain constant temperature (25 ℃) and avoid a critical increase in reaction temperature.

The concentration (C) of CP in the solution is analyzed over time, using high performance liquid chromatography coupled with UV detection (HPLC-UV), with a Shimadzu Corporation apparatus (Nexera model, Tokyo, Japan) equipped with a Shimpack GISS-HP C18, 3 μm column (100 ×3.0 mm I.D.), a pump LC-30 CE, an Autosampler SIL-30AC, an Oven CTO-20AC, a Degasser DGU-20A5r, a System Controller CBM-20 A Lite and a Diode Array Detector (SPD-M20A). The injection volume was 40 μL and column temperature was set at 30℃. The mobile phase consisted of a 60:40 mixture of water and acetonitrile, respectively, with a total flow of 0.2 mL/min. The wavelength set for detection was 193 nm. The H_2O_2 consumption was also monitored following a method based on the formation of a yellow complex ($[Ti(OH)_3(H_2O_2)]^+$) between hydrogen peroxide and Ti^{4+} (from titanium oxysulfate (IV), $TiOSO_4$). The reaction needs to take place at acidic pH, with a solution of 0.5 M H_2SO_4. The complex formed has an absorption maximum at 404 nm [34].

The stability of the catalysts is discussed in terms of the Fe and Cu concentrations leached, determined by inductively coupled plasma optical emission spectroscopy (ICP-OES). The equipment used is an ICP-OES spectrometer Perkin Elmer Optima 8300. Catalyst reusability was studied for the best catalyst during three consecutive cycles, under the optimal pH pre-established. For this purpose, once the reaction was finished, the catalyst is separated by filtration with a cellulose membrane, with a pore size of 0.45 μm. Later, it is washed with a 0.05 M NaOH solution, to desorb organic acids that could still be adsorbed on the catalyst. The next step is to wash it with abundant Milli-Q water until neutral pH of filtrated water and finally, the catalyst is dried at 100 ℃ overnight and reused in consecutive cycles, maintaining a catalyst loading of 0.5 g/L and the rest of the operational parameters.

2.5. Cell culture and cytotoxicity evaluation

Human embryonic kidney cell line HEK-293 were purchased from the CIC (Centro de Instrumentación Científica) of the University of Granada, Spain. HEK-293 were grown in DMEM medium (Thermo Fischer Scientific, MA, USA) supplemented with 10% fetal bovine serum (FBS; Thermo Fischer Scientific, MA, USA) and 1% penicillin-streptomycin antibiotics (Thermo Fischer Scientific, MA, USA). The cells were seeded at a concentration of 8000 cells/well in 96 well/plates and 30 000 cells/well in 12 well plates and maintained in complete medium at 37 °C, 5% CO_2 and 60% humidity in incubator for 24 h before adding the different samples. 96-well/plates were used for MTS viability assay, while the 12-well/plates were used for optical imaging microscopy. The different solution to test were added in triplicate at 4 different dilutions (1%, 2%, 10% and 25%). After 24 h incubation, 20 μL of MTS (CellTiter 96 AQ_{ueous} One Solution Cell Proliferation Assay, Promega, WI, USA) were added to each well and its absorbance was measured at 490 nm with a plate-reader. For optical microscopy, images were acquired with an objective 10x with an inverted microscope (Leica Microsystems, Germany).

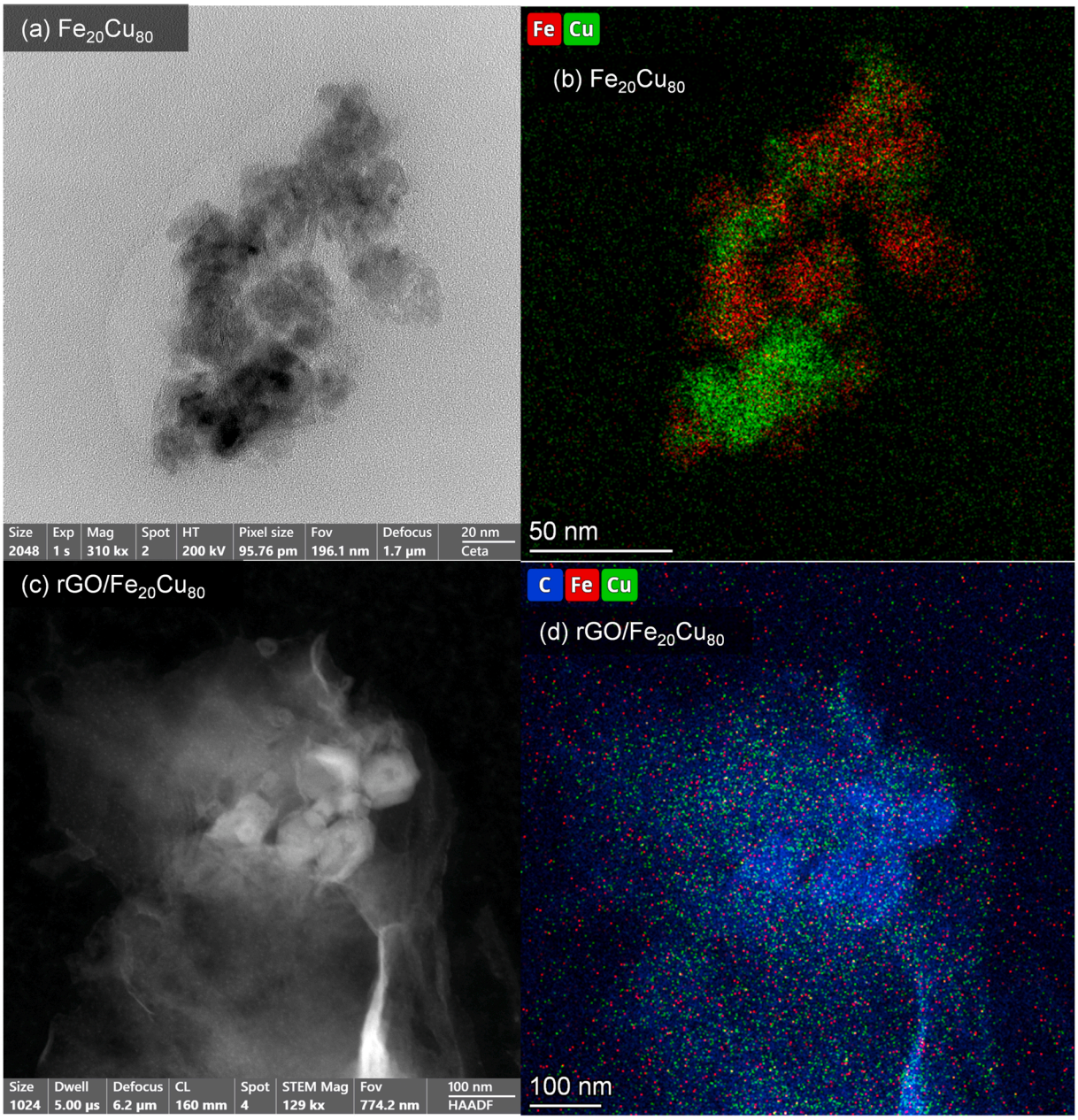

Fig. 2. a) STEM image and b) microanalysis of $Fe_{20}Cu_{80}$ catalyst; c) STEM and d) microanalysis of rGO/$Fe_{20}Cu_{80}$ catalyst.

3. Results and discussion

3.1. Materials characterization

The metal loading in the rGO/ bimetallic Fe_xCu_y catalysts was determined from the TG analysis. The TG/DSC profiles of samples are showed in Fig. S1, supporting information). Both TG and DSC profiles are quite similar, denoting the importance of the support transformations. Below 200 ºC the dehydration process occurs, producing a weight loss of around 20% denoted also by a marked endothermic process in the DSC profile. At this temperature the carbon support is then oxidized, the sample weight deeply decreased without a significant temperature increase, thus also leading to a sharp exothermic peak in the DSC profile. The combustion of the most aromatic/graphitic rests (more thermally stable) occurs at around 430–450 ºC, however because the amount of carbon is low, and the combustion slower, the second exothermic peak in the DSC profile are wider. The remaining solid correspond to a mixture of metal oxides. The accumulated weight loss always exceeds 99.3–99.5%, in good agreement with the expected metal loadings (0.2% wt.). The morphology of the samples was studied by SEM images (Fig. 1). The morphology of $Fe_{40}Cu_{60}$ (Fig. 1a) consists of agglomerated nanoparticles with spherical shape. In the case of the rGO/FeCu catalysts, the morphology of the sample is clearly dominated by the layered structure of rGO support (Fig. 1b).

TEM images (Fig. 2) were used to analyze the phase distribution. The polycrystalline character of the spherical particles observed by SEM was pointed out for the bimetallic Fe_xCu_y – oxide catalysts ($Fe_{20}Cu_{80}$ as an example in Fig. 2a). The characteristic planes of the nanocrystal structures were also determined (figure not shown). In this case, most of them were quantified around 2.4 Å, which are characteristic of plane (111) of copper oxide (Cu_2O) structure. In general, EDX microanalysis (Fig. 2b) confirms that Fe and Cu were not homogeneously distributed in the unsupported catalysts, and areas (microcrystals) with predominant Fe or Cu concentration were detected. In the case of rGO/$Fe_{20}Cu_{80}$ catalyst

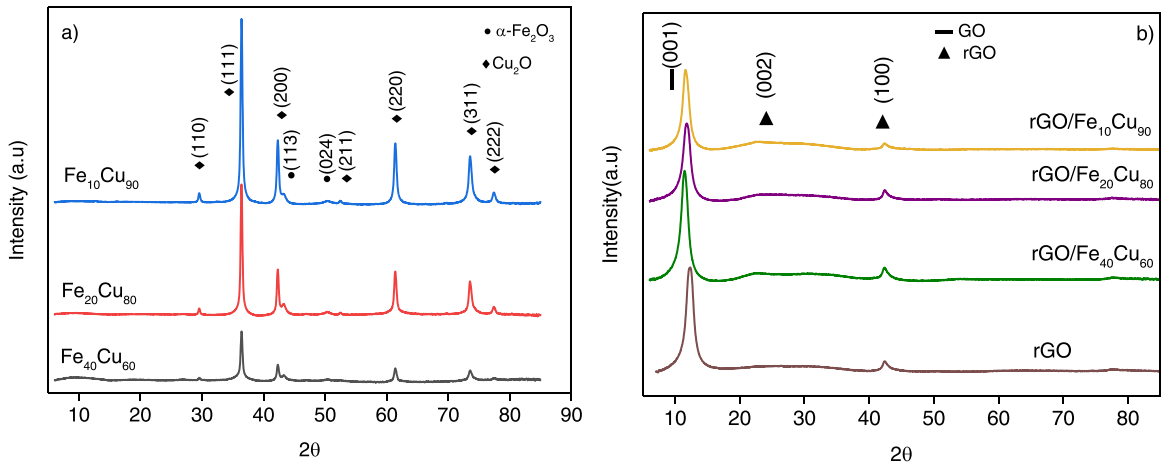

Fig. 3. Diffractograms of a) unsupported catalysts and b) supported catalysts.

Table 1
pH_{pzc} and textural parameters of the catalysts.

Sample	pH_{pzc}	S_{BET} (m^2/g)	V_T (cm^3/g)	V_{meso} (cm^3/g)
$Fe_{40}Cu_{60}$	7.28	39	0.147	0.114
$rGO/Fe_{40}Cu_{60}$	3.77	49	0.055	0.031
$Fe_{20}Cu_{80}$	7.33	32	0.118	0.092
$rGO/Fe_{20}Cu_{80}$	3.62	36	0.080	0.050
$Fe_{10}Cu_{90}$	7.81	22	0.076	0.060
$rGO/Fe_{10}Cu_{90}$	3.97	39	0.062	0.035
rGO	3.45	55	0.090	0.060

(Fig. 2c, d) the predominant phase is the rGO support, and the particle size of Fe and Cu nanocrystals is strongly reduced. In this case, no agglomeration of phases was detected and both metals were homogeneously distributed on the support, probably favored by strong interactions and the low metal loading used (0.2% wt.).

Fig. 3a and b shows the XRD patterns of bimetallic Fe_xCu_y and rGO/bimetallic Fe_xCu_y catalysts, respectively. Fig. 3a shows that unsupported nanoparticles present always well-defined diffraction peaks, while in the case of the supported ones (Fig. 3b), only the peaks associated to both GO and rGO structures were detected [35]. Fig. 3a shows that the intensity of the peaks (crystallinity) increased with the Cu-content in the bimetallic catalysts. This effect could be associated with the formation of Cu_2O crystal as previously observed by TEM (Fig. 2b). Peaks observed at 29.56°, 36.42°, 42.32°, 52.45°, 61.40°, 73.54° and 77.38° correspond to (110), (111), (200), (211), (220), (311) and (222) diffractions of the Cu_2O structure (JCPDS no. 05–0667). Although the peaks at 43.26° and 50.28° were assigned to planes (113) and (024) of the α-Fe_2O_3 structure (JCPDS carta no. 33–0664), clearly this component is less crystalline than the copper-one or remains amorphous [36]. The crystallinity clearly increased with the Cu-content as denoted the strong increase of the peak intensity, thus, the particle crystal size of CuO_2 phase (calculated by applying the Scherrer equation), although are significantly high in all cases increased from 34.7 to 44.5 nm for $Fe_{40}Cu_{60}$ and $Fe_{10}Cu_{90}$ catalysts, respectively. Nevertheless, the formation of mixed Fe-Cu oxides as $CuFe_2O_4$ spinels (JCPDS No. 00–034–0425) is not achieved (Fig. 3a).

Regarding de rGO-bimetallic catalysts (Fig. 3b), the diffraction angles may correspond to the inter-layer distance between graphitic sheets [37]. The peak of rGO/bimetallic Fe_xCu_y catalysts at approximately 12° was associated to the reflection for the (001) plane of GO [38]. The diffraction peaks that appeared at ca. 26.8 and 43.5°, associated to plane (002) and (100) respectively, corresponds to the lowest inter-layer distance between the graphite sheets, confirming the removal of oxygenated groups during the synthesis of catalysts and the formation of rGO. The peaks associated of iron and copper species were not observed in the XRD patterns of rGO bimetallic catalysts probably due to the low content of Cu and Fe present in the samples (i.e., 0.2% wt.).

The pH_{PZC} for Fe_xCu_y and rGO/Fe_xCu_y catalysts are listed in Table 1. The results show that rGO/ Fe_xCu_y catalysts present an acidic character, with pH_{pzc} around 3.5, due to the presence of some acidic functional groups in the surface of rGO, comprising mainly epoxy and carboxyl

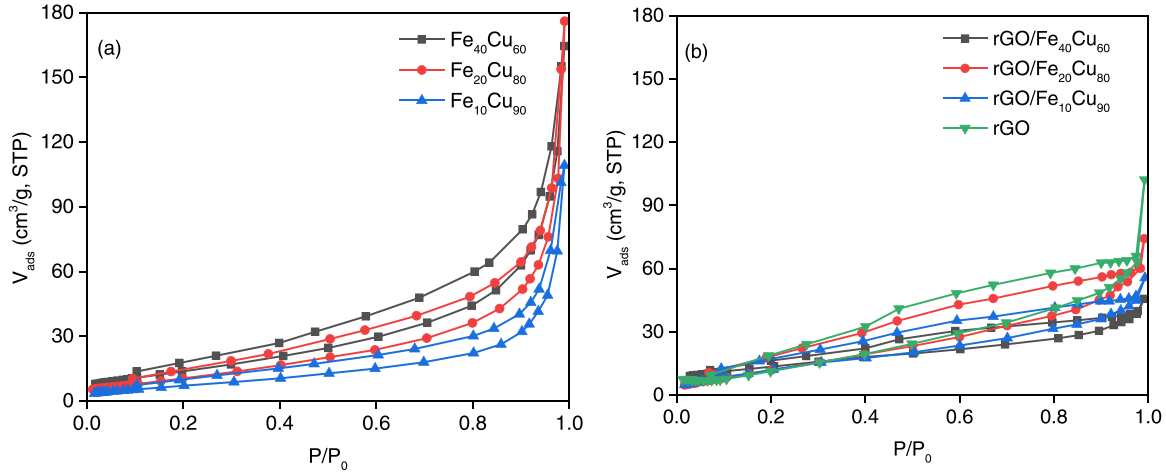

Fig. 4. Adsorption-desorption isotherms for a) unsupported catalysts and b) rGO supported catalysts.

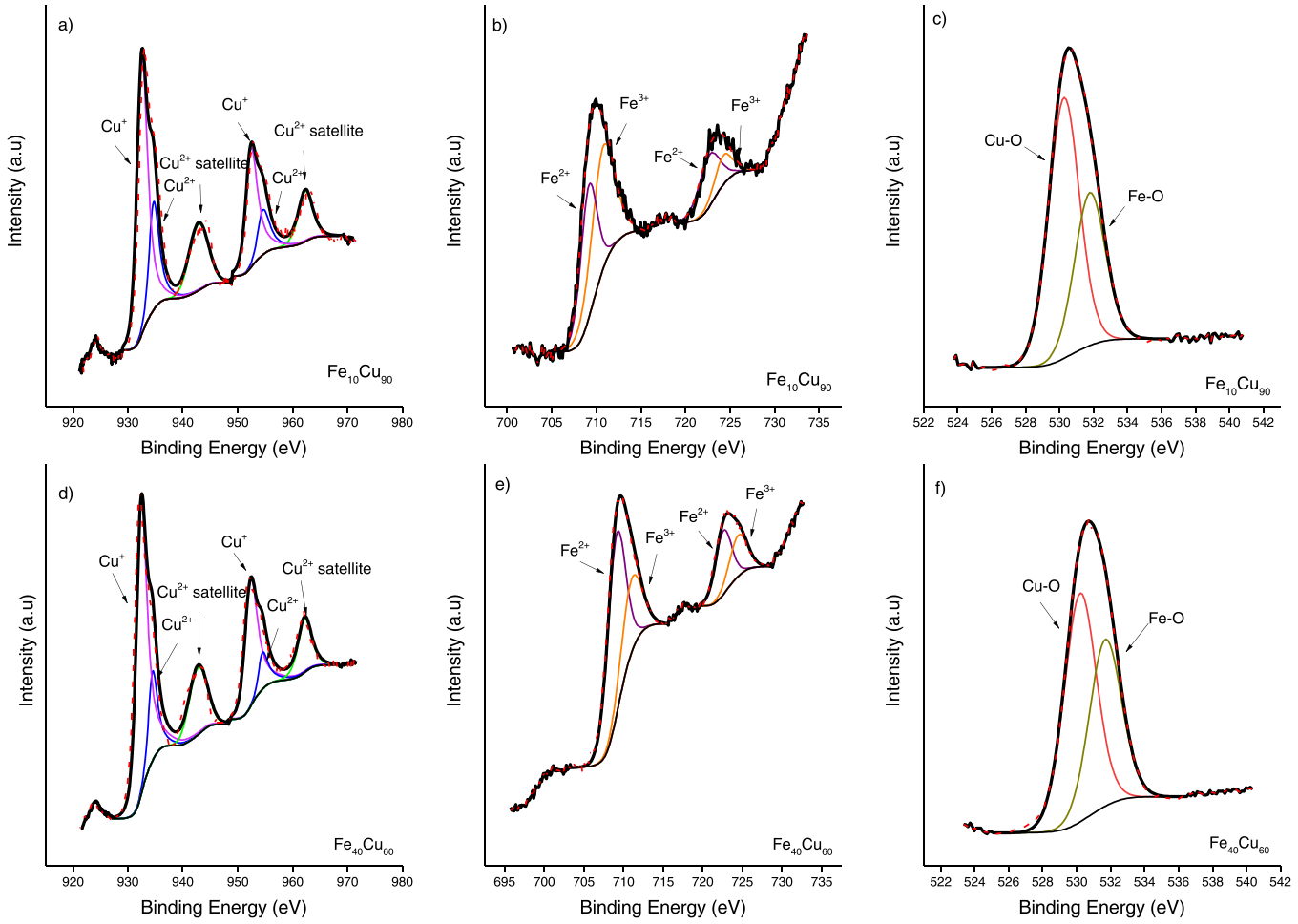

Fig. 5. Cu_{2p} deconvoluted spectra, Fe_{2p} deconvoluted spectra and O_{1s} deconvoluted spectra for $Fe_{10}Cu_{90}$ (a, b and c, respectively) and $Fe_{40}Cu_{60}$ (d, e and f, respectively).

Table 2
Atomic and species percentages and their binding energies (in brackets, eV), based on XPS analysis.

Sample	Fe (%)	Cu (%)	C (%)	O (%)	Fe (%)		Cu (%)		O (%)			
					Fe^{2+}	Fe^{3+}	Cu^{+}	Cu^{2+}	C-O	C═O	Fe-O	Cu-O
$Fe_{10}Cu_{90}$	3	24.2	–	72.8	43.3 (709.1)	56.7 (710.8)	80 (932.4)	20 (934.4)	–	–	37 (531.8)	63 (530.3)
$Fe_{40}Cu_{60}$	8.5	12.6	–	78.9	68.5 (709.1)	31.5 (711)	72.9 (932.5)	27.1 (934.6)	–	–	57.8 (531.7)	42.2 (530.2)
					C%				O(%)			
					C-C	C-O	C═O		C-O	C═O		
rGO/ $Fe_{10}Cu_{90}$	–	–	72.8	27.16	52.4 (284.6)	38.1 (286.6)	9.5 (288.6)		89.6 (532.1)	10.4 (530.6)		
rGO/ $Fe_{40}Cu_{60}$	–	–	73.3	26.7	57.5 (284.6)	30.9 (286.6)	11.6 (288.4)		95 (532.5)	5 (530.4)		

groups, among others [39,40]. For unsupported catalysts, their pH_{pzc} is found around 7, although slowly increased with increasing the Cu-content [41]. Thus, the pH_{pzc} for supported catalysts are slightly higher than the support and also increased up to values close to 4 at high Cu-content (i.e., rGO/$Fe_{10}Cu_{90}$).

The textural characterization of catalysts was evaluated by physisorption of N_2 at – 196 °C. Fig. 4a-b shows the N_2 adsorption-desorption isotherms of Fe_xCu_y and rGO/Fe_xCu_y, respectively. The surface areas (S_{BET}) of Fe_xCu_y catalysts ranges between 20 and 40 $m^2\ g^{-1}$ (Table 1). In general, the isotherms can be classified of type-III for non-porous solids, in accordance with IUPAC classification [42], although a certain adsorption with increasing P/P_0 indicates the presence of mesopores in the samples, associated to interparticle voids. S_{BET} and V_T increased with increasing the Fe-content in the composite, probably due to a smaller crystallinity, as previously commented (Table 1). The supported rGO/-Fe_xCu_y catalysts always present higher S_{BET} and V_T than their corresponding Fe_xCu_y catalysts, but decreased regarding rGO, indicating that the nanoparticles are partially blocking the porosity of the support. Mainly, the changes in the isotherm shape for supported catalysts (Fig. 4b) are associated to the development of larger hysteresis cycles at lower P/P_0, confirming the formation of smaller mesopores.

X-ray photoelectron spectroscopy (XPS) measurements were also carried out for some of the catalysts, ie., $Fe_{10}Cu_{90}$, $Fe_{40}Cu_{60}$, rGO/$Fe_{10}Cu_{90}$ and rGO/$Fe_{40}Cu_{60}$. The results are shown in Fig. 5 for unsupported catalysts and Table 2 collected atomic percentages for Fe, Cu, C and O for the catalysts studied, along with their species distribution and binding energy. It is noteworthy that the atomic Fe/Cu ratios detected by XPS are in agreement with those expected according to the fitted bulk

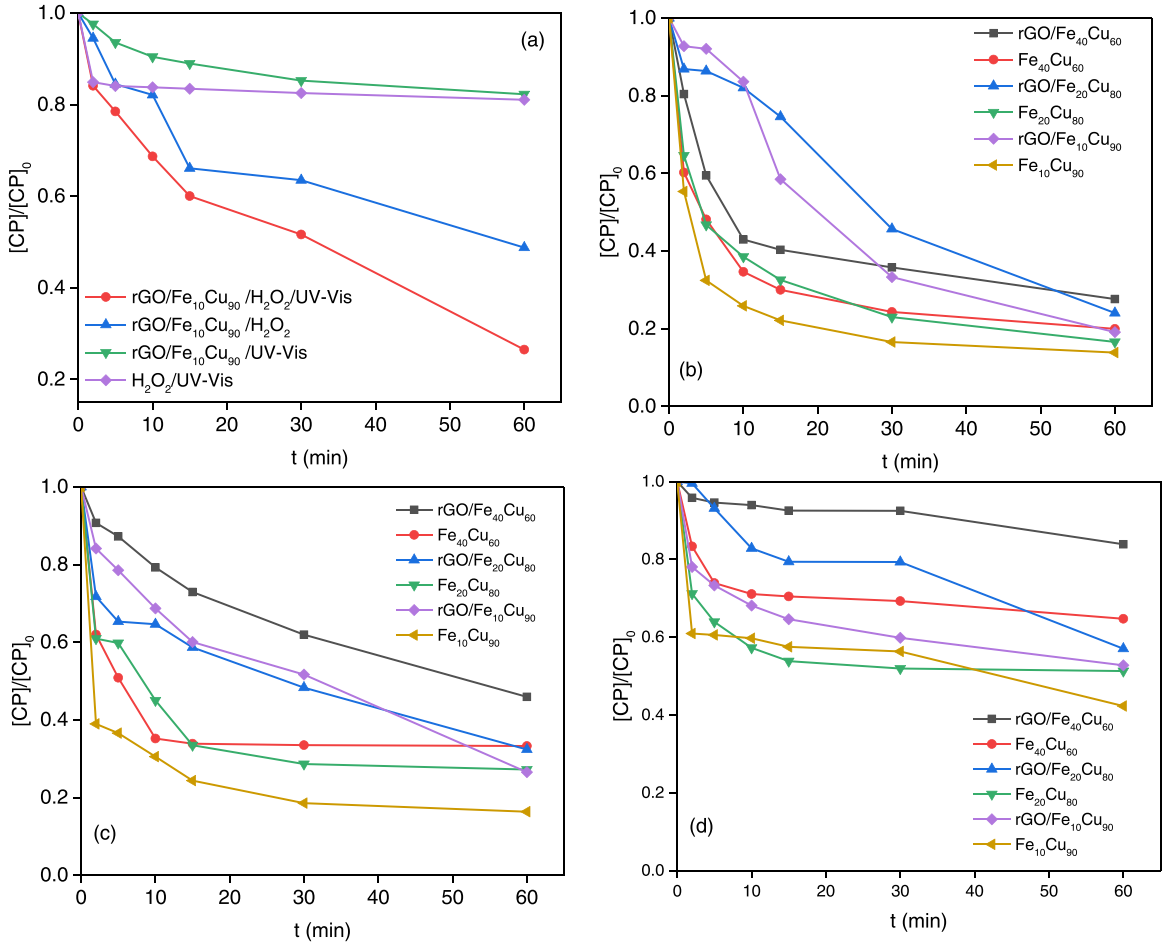

Fig. 6. a) CP degradation using rGO/$Fe_{10}Cu_{90}$ sample at different operating conditions and pH 6; CP degradation using the photo-Fenton process with supported and unsupported catalysts at b) acidic pH, c) natural pH and d) alkaline pH.

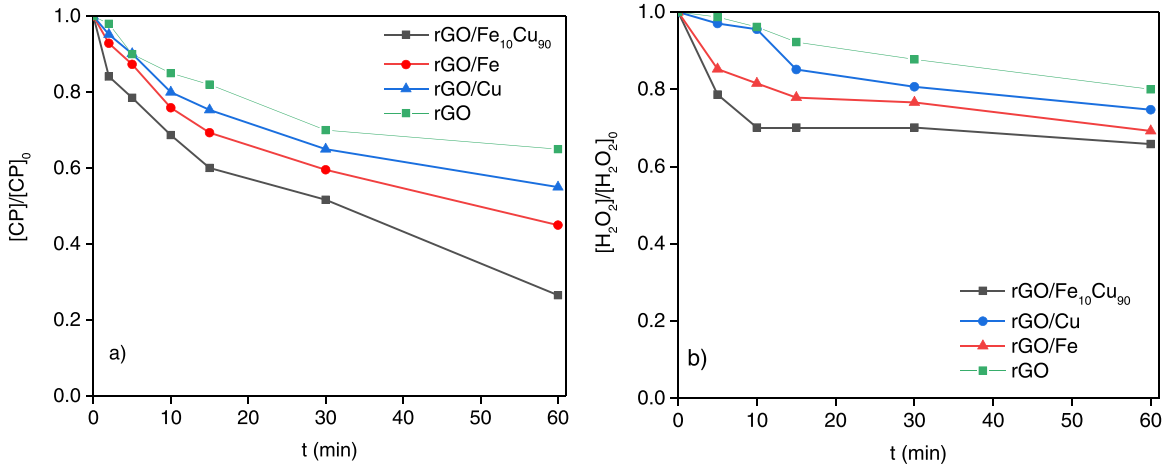

Fig. 7. a) CP degradation and b) H_2O_2 consumption for rGO/$Fe_{10}Cu_{90}$, rGO/Cu, rGO/Fe and rGO at natural pH.

composition (1/9 and 1/1.5 for $Fe_{10}Cu_{90}$, $Fe_{40}Cu_{60}$, respectively), and also that the total oxygen content increase with the Fe-portion, because of the greater oxygen content of these oxides regarding copper oxides. Results also agree with those obtained by HRTEM/EDX and DRX, indicating that both phases remain independent. Fig. 5a shows the deconvoluted Cu_{2p} XPS spectra for $Fe_{10}Cu_{90}$ and $Fe_{40}Cu_{60}$ exhibiting two main bands located at around 932.4 and 952.4 eV, respectively corresponding to $Cu_{2p3/2}$ and $Cu_{2p1/2}$ spin-orbital splitting photoelectrons. Deconvolution reveal the presence of Cu^{+} and Cu^{2+} by the components at 932.4 and 934.4 eV respectively. These peaks are associated with two satellite bands located at higher binding energy. The deconvoluted Fe_{2p} XPS spectra for $Fe_{10}Cu_{90}$ and $Fe_{40}Cu_{60}$ are shown in Fig. 5b. Similarly, two broad peaks at around 711.5 and 725.1 eV were observed corresponding to $Fe_{2p3/2}$ and $Fe_{2p1/2}$. The results also reveal the presence of both Fe^{2+} and Fe^{3+} species at 709.1 and 710.8 eV respectively. It is noteworthy that the ratio Fe^{+2}/Fe^{+3} increased from 0.75 to 2.22 when

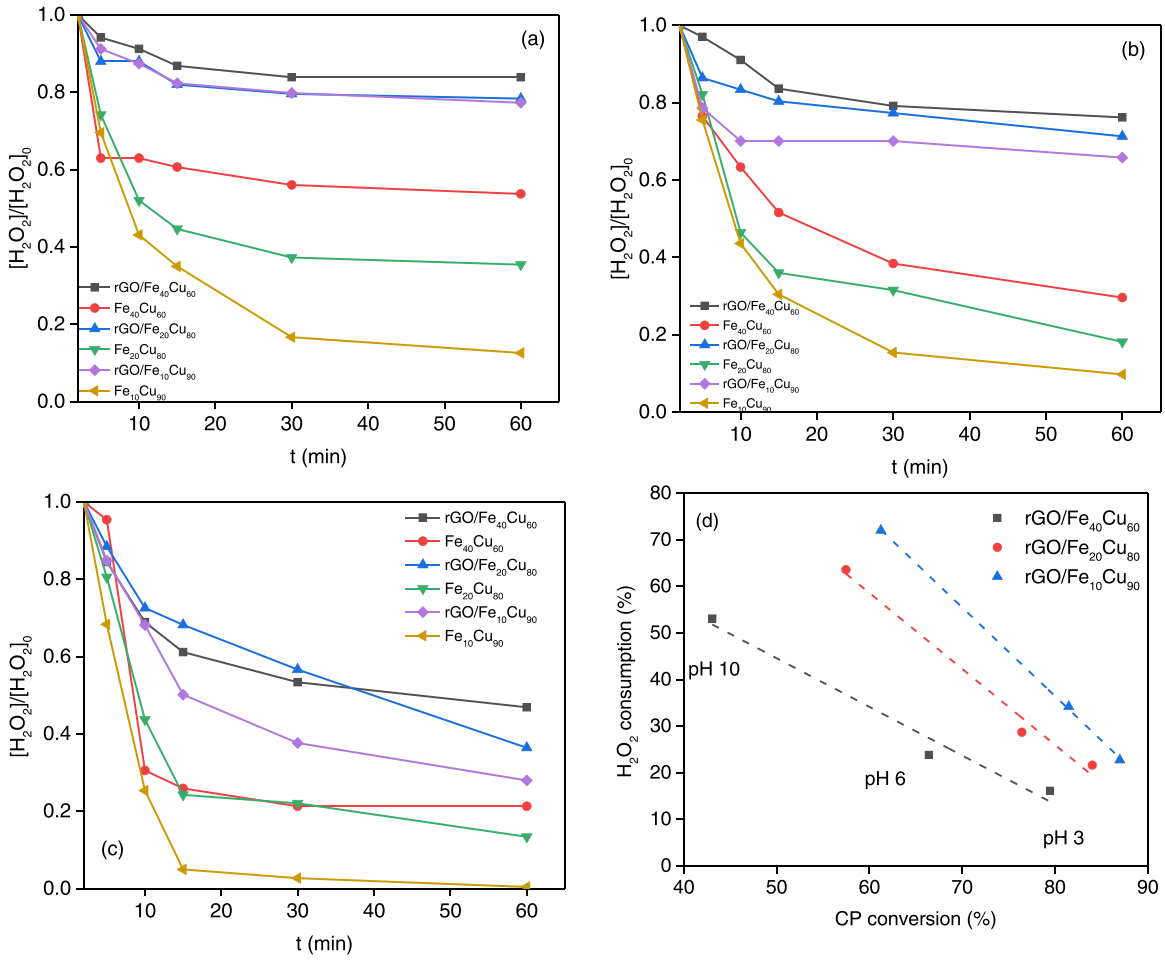

Fig. 8. Study of H_2O_2 consumption for all catalysts at different pH values with the photoFenton process, a) acidic pH, b) natural pH, c) alkaline pH, d) relationship between the CP conversion and H_2O_2 consumed.

the ratio Fe/Cu in the bimetallic catalysts increased from 1/9–4/6 ($Fe_{10}Cu_{90}$ vs $Fe_{40}Cu_{60}$), while the contrary tendency is observed for the ratio Cu^+/Cu^{2+}. This is, the reduction of Fe^{3+} to Fe^{2+} seems not be favored by the Cu-content, but on the contrary, the large Cu_2O crystallite size observed in this sense (DRX, TEM) could limit the electronic transfers.

The deconvolution of O1s spectra for both catalysts (Fig. 5c and d) confirms the presence of O in Cu-O at ca. 530.3 eV as well as the oxygen in Fe-O at 531.8 eV. Regarding supported catalysts, XPS results are unable to detect a significant signal of metals (as occurs in the DRX analysis), probably because metals could be located inside the interlayer voids. Only the $C_{1\,s}$ and O_{1s} regions of the rGO/$Fe_{10}Cu_{90}$ and rGO/$Fe_{40}Cu_{60}$ samples are treated (Table 2). The C_{1s} XPS spectrum (not shown) exhibits three major peaks associated with three different types of carbon bonds with binding energies at 284.6 (assigned to C-C or C-H), 286.6 (assigned to C-O) and 288.6 eV (assigned to C═O) as previously reported [43,44]. In the case of the $O_{1\,s}$ spectrum of both rGO/$Fe_{10}Cu_{90}$ and rGO/$Fe_{10}Cu_{90}$ samples, they can be deconvoluted into two components at ca. 530.5 and 532.4 eV, corresponding to C-O bonds and C═O bonds (Table 2).

3.2. Degradation of CP with the photoFenton process

The selection of the operational conditions for CP degradation was carried out using the rGO/$Fe_{10}Cu_{90}$ catalyst (Fig. 6a). These experiments were carried without a fitted pH (the natural pH of solutions is around 6). In the absence of catalyst, wet oxidation using H_2O_2 as $OH^{\bullet}$ source and photolysis under UV-Vis radiation (H_2O_2/UV-Vis) trigger a CP degradation of around 15%. The catalyzed degradation of CP obtained after 1 h of UV-Vis irradiation (rGO/$Fe_{10}Cu_{90}$/UV-Vis) was very similar. Conversion increased in Fenton-like process (rGO/$Fe_{10}Cu_{90}$/H_2O_2) up to around 50% of the initial CP concentration, being also finally favored by the presence of UV-Vis radiation in the photo-Fenton-like process (rGO/$Fe_{10}Cu_{90}$/H_2O_2/UV-Vis) achieving conversion values close to 80% at natural pH (Fig. 6a).

Nevertheless, it is well known that Fenton process is dependent on pH, mainly working at acidic pH (around 2.8–3.0) [14]. Once the adsorption-desorption equilibrium was reached, the influence of pH on the photo-Fenton-like process was studied with all prepared catalysts at different pH value (Fig. 6b, c and d for acidic, natural and alkaline pH, respectively). In general, the results showed a slightly lower CP degradation for the rGO supported catalysts in comparison with the unsupported bimetallic catalyst. Nevertheless, these results should be analysed taking into account the low metal loading content of the supporting rGO materials (ca. 0.2% wt.). The small differences observed in the total conversion after 60 min of reaction pointed out [45] that the activity of these supported metal nanoparticles becomes strongly favoured after deposition in rGO. In both catalysts series it is observed that: i) activity increased with the Cu ratio in the catalyst (the highest CP degradation was achieved with $Fe_{10}Cu_{90}$); and ii) increasing pH value the CP conversion decreased, this effect is higher for catalysts with lower Cu-content. Thus, Cu_2O not only favours the catalytic activity, but also allows to increase the pH range maintaining activity, and thus, avoiding the acidification processes [46,47]. Using $Fe_{10}Cu_{90}$ nanoparticles the CP degradation is higher than 80% even at natural pH, remaining superior to 60% even in basic conditions, while under these conditions the

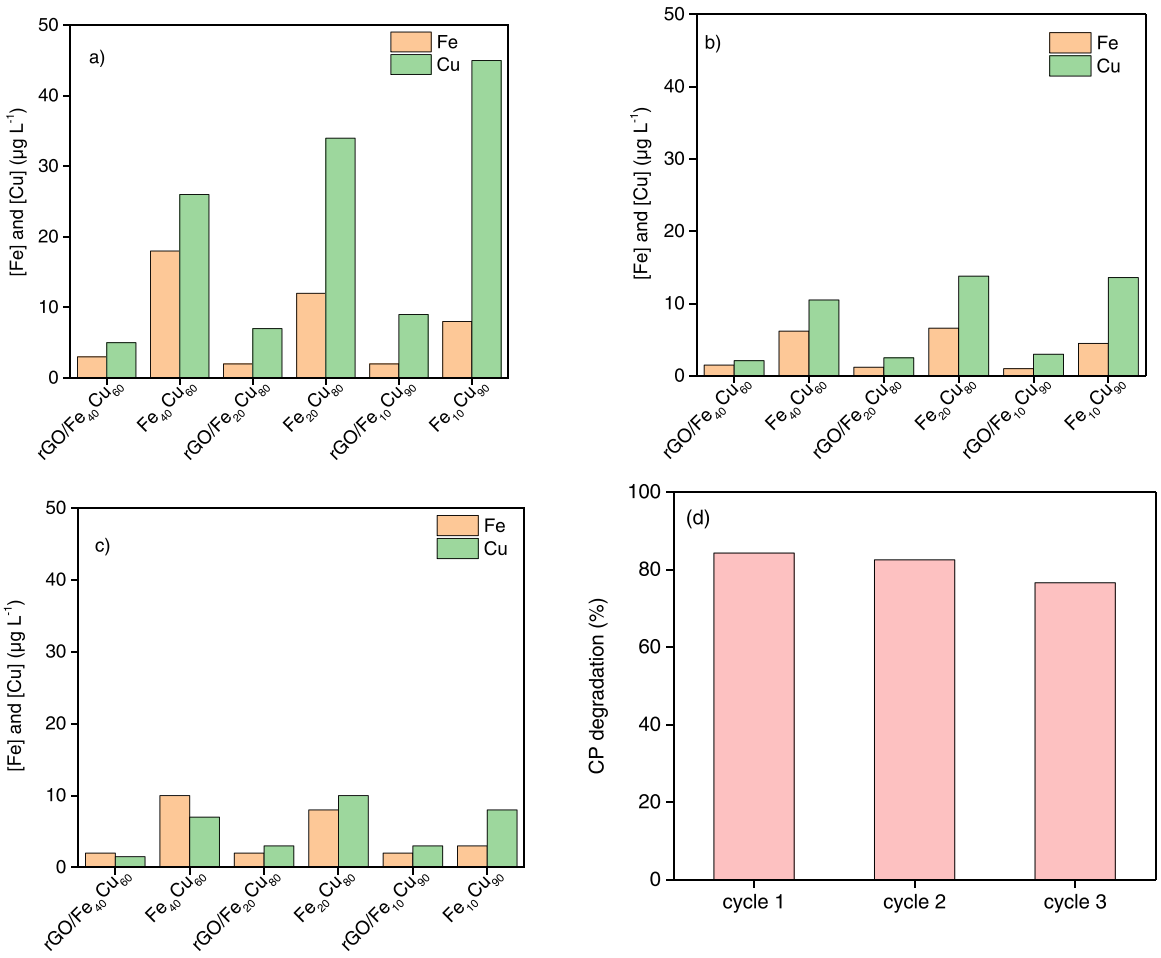

Fig. 9. Study of Fe and Cu leached for all catalysts with photoFenton process at different pH values, a) acidic pH, b) natural pH, c) alkaline pH; d) CP degradation during three consecutive cycles using photo-Fenton process and rGO/$Fe_{10}Cu_{90}$ sample.

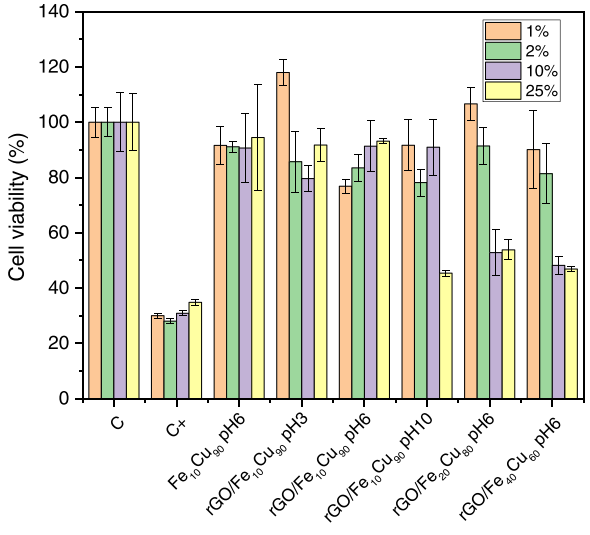

Fig. 10. Cell Viability: cell viability of HEK-293 after 24 h of exposure to the different coping was tested by MTS assay. The compound was added at different concentrations/dilutions (1%, 2%, 10% and 25%) and after 24 h the MTS assay was performed. Negative control (NEG) are non treated cells, while positive control (POS) are cells with 20% EtOH. Each compound was tested in triplicate (n = 3 wells/condition) and the results represent the average and standard deviation.

catalyst $Fe_{40}Cu_{60}$ only reached the 35% of CP degradation.

Fig. 7a and b show the CP degradation and the H_2O_2 consumption, respectively for the rGO/$Fe_{10}Cu_{90}$ catalysts, bare rGO and the monometallic catalysts (namely rGO/Fe and rGO/Cu with a similar metal loading, 0.2% wt.). The highest CP degradation was obtained for the supported bimetallic catalyst, i.e., rGO/$Fe_{10}Cu_{90}$ confirming the synergetic effects between rGO and bimetallic particles with respect to the monometallic catalysts.

The efficiency of the process also depends on the H_2O_2 consumption and the stability of the catalysts allowing their reuse. Thus, along with CP degradation, the H_2O_2 consumption was also monitored in all the experimental conditions (Fig. 8). Fixing the pH of solution, H_2O_2 consumption increases in the same order than CP degradation, i.e., with increasing the Cu-content of the catalyst. Differences are smaller at low pH values using supported catalysts, probably related with their acidic character, nevertheless, consumption clearly increased with increasing the basicity of the solution, pointing out the importance of the catalyst composition on their performance under neutral/basic conditions. With increasing the pH values, the CP conversion decreased, but the H_2O_2 consumption increased, favored also by decomposition processes into H_2O and O_2, thus avoiding the formation of $OH^{\bullet}$ [15,16].

Fig. 8d showed the relationship between CP and H_2O_2 conversion obtained with each supported bimetallic catalysts at the different pH values. The results show that when the Cu content increase in the catalyst, the slope of the line increased, indicating therefore a higher H_2O_2 consumption for the same CP conversion. Rich Cu-catalysts therefore are more active also in neutral/basic conditions, but also induce a larger and faster H_2O_2 consumption. In fact, the H_2O_2

Table 3
Compilation of recently published works regarding bimetallic FeCu-catalysts supported on carbon materials using PhotoFenton process.

Catalyst	Metal loading	Pollutant and concentration	Degradation obtained and time	Ref.
FeCu/oxidized nanodiamonds	0.2%	Phenol, 100 mg/L	100%, 2 h	[48]
FeCu/rGO	10%	Norfloxacin, 10 mg/L	96%, 1 h	[47]
FeCu/rGO	0.2%	Phenol, 100 mg/L	100%, 4.5 h	[48]
FeCu/GO	20%	Dichlorodiphenyltrichloroethane, 10 mg/L	100%, 3 h	[49]
FeCu/rGO	0.2%	Cyclophosphamide, 20 mg/L	82%, 1 h	This work

concentration becomes negligible using the $Fe_{10}C_{90}$ catalyst after only 15 min of reaction (Fig. 8c).

Together with the efficiency of the catalysts, another important issue is their stability. Fig. 9a, b and c summarized the results of the concentration of metals leached from catalysts at different pH conditions. It is noteworthy that in all cases the metal content clearly complies with the legislation, the higher contents were detected around 45 μg/L of Cu leached from $Fe_{10}Cu_{90}$ unsupported nanoparticles under acidic conditions, while as commented, limits are stablished in 2 mg/L. Leaching evidently decreased with increasing the pH of the solutions, being at neutral or basic conditions quite similar between catalysts.

The rGO/$Fe_{10}Cu_{90}$ catalysts was chosen as the best catalyst, due to its previously described characteristics, its reusability was analyzed over three consecutive cycles (Fig. 9d). CP degradation is reduced slowly but gradually over the cycles, majorly due to the loss of Fe and Cu active sites because of leaching, and the possible adsorption of byproducts on the rest of active sites of the catalyst, that were not desorbed during the rinsing process. This reduction of active sites and therefore, catalyst deactivation, causes less formation of radicals from H_2O_2, which subsequently slightly diminishes degradation over the cycles. It is noticeable that the leaching is more prominent in the case of Cu (because is the predominant phase, results not shown), which could be responsible to a larger extent for the reduction in degradation during the cycles. This also confirms that the influence of the homogeneous catalysis (from leached metals) with this catalyst series is scarce, taking into account the low leaching occurred. So, it is feasible to conclude that the catalyst rGO/$Fe_{10}Cu_{90}$, at its natural pH, can be reused during three consecutive cycles, still maintaining an activity above 75%.

In spite that characterization results pointed out that both metals remain forming independent nanocrystals, the synergetic role between them for the CP degradation is clearly pointed out as previously observed (Fig. 7a). The semiconductor character of rGO induces a significant photoactivity, and in spite of all the previously results showed that activity increased with the Cu/Fe ratio in bimetallic catalysts, the performance of monometallic indicates that rGOFe > rGOCu. This result shows that the presence of Cu^{+} in the bimetallic catalysts favors the reduction of Fe^{+3} increasing the redox cycles of the pairs Cu^{+}/Cu^{+2} and Fe^{+2}/Fe^{+3}, the generation of $OH^{\bullet}$ and the consequent catalytic activity. The rGO support also enhanced the electronic transfer between phases and allows decrease the leaching degree, thus obtaining highly active and stable bimetallic catalysts even at low pH values and avoiding the acidification traditionally needed in Fenton reactions.

Regarding the cytotoxicity of the degradation by-products, the results obtained from the cell viability assay on the kidney cell line HEK-293 (Fig. 10) after 24 h of incubation with the different solutions, display a negligible and very low toxicity at low concentrations (1% and 2% dilutions) for all the tested chemicals. Interestingly, at a dilution of 10%, final aqueous solutions from both rGO/$Fe_{20}Cu_{80}$ and rGO/$Fe_{40}Cu_{60}$ samples at pH 6 showed a significant decrease in cell viability, also visible by the cell morphology in Supplementary Fig. S2 (typical of dead cells). The toxic effect of the aqueous suspension was also confirmed for the dilution of 25% (the highest concentration tested), at which final solution from CP degradation using rGO/$Fe_{10}Cu_{90}$ sample at pH 10 also showed a compromised cell viability. This cell line was chosen by taking into account the main negative effect the tested compounds might have on kidneys. It is noteworthy that the by-products obtained from rGO/$Fe_{10}Cu_{90}$ sample at both neutral and acid pH showed a high cell viability.

Table 3 compared the results from literature with those obtained in the present work regarding different FeCu bimetallic nanoparticles supported on carbon materials using the photoFenton process [47–49]. In general, the results obtained with our best catalyst (rGO/$Fe_{10}Cu_{90}$, at 0.2% wt.) are similar or enhance those obtained in the literature, taking into account that in general, the total degradation of the other pollutants was achieved in around 2–3 h (even with loadings as high as 20%), while in our case, we were able to achieve more than 80% degradation of a cytostatic compound (more recalcitrant) in an hour, at near-neutral pH and with a loading of 0.2% of metal.

4. Conclusions

Bimetallic Fe_xCu_y - oxide catalysts were synthesized with different molar proportions (i.e., $Fe_{40}Cu_{60}$, $Fe_{20}Cu_{80}$ and $Fe_{10}Cu_{90}$), supported on rGO with a metal loading of 0.2% wt. Both series of catalysts presented some mesopores, with supported catalysts showing a higher S_{BET}, around 40 m^2/g. Their activity was evaluated on the degradation of an aqueous solution of the antineoplastic drug, cyclophosphamide, CP using the photoFenton process under UV-Vis irradiation. rGO/$Fe_{10}Cu_{90}$ sample was confirmed as the best catalyst under natural pH, avoiding acidification processes while achieving around 80% removal of the pollutant. With increasing the Cu content in the catalyst, the H_2O_2 consumption increased for the same CP conversion. Rich Cu-catalysts therefore are more active also in neutral/basic conditions, but also induce a larger and faster H_2O_2 consumption. The stability of the samples was studied in terms of their Fe and Cu leaching and their reusability, where rGO/$Fe_{10}Cu_{90}$ showed Fe and Cu concentrations on solution below European Union requirements for water consumption and it can be reused during three consecutive cycles with an activity higher than 75%. Regarding the cytotoxicity of the degradation by-products, overall, the results display a very low toxicity effect of the compounds, especially at low concentrations, with some significant effects on cell viability only for the highest concentration tested.

CRediT authorship contribution statement

L.T. Pérez-Poyatos: Investigation, Conceptualization, Formal analysis, Methodology, Writing – original draft. **L.M. Pastrana-Martínez:** Conceptualization, Data curation, Resources, Writing – review & editing, Supervision. **S. Morales-Torres:** Conceptualization, Data curation, Resources, Writing – review & editing, Supervision. **P. Sánchez-Moreno**: Investigation, Methodology, Writing – review. **M. Bramini:** Investigation, Methodology, Writing – review. **F.J. Maldonado Hódar**: Conceptualization, Resources, Project administration, Funding acquisition, Writing – review & editing, Supervision.

Declaration of Competing Interest

The authors declare that they have no known competing financial interests or personal relationships that could have appeared to influence the work reported in this paper.

Acknowledgements

This work was financially supported by the FEDER/Junta de Andalucía-Consejería de Transformación Económica, Industria, Conocimiento y Universidades/B-RNM-486-UGR20 and project PCI2020–112045 from MCIN/AEI/10.13039/501100011033 and European Union Next Generation EU/PRTR, as part of the PRIMA Programme (Nano4Fresh project). S.M.T. (RYC-2019–026634-I), L.M.P.M. (RYC-2016–19347) and M.B. (RYC2019–027692-I) acknowledge the MICIN/AEI/10.13039/501100011033 and the European Social Found (FSE) "El FSE invierte en tu futuro" for Ramón y Cajal research contracts. P.S.M. acknowledges Ministerio de Ciencia e innovación y la Agencia Estatal de Investigación a través del programa Juan de la Cierva Incorporación (IJC2018–036305-I). Funding for open access charge: Universidad de Granada / CBUA

Appendix A. Supporting information

Supplementary data associated with this article can be found in the online version at doi:10.1016/j.cattod.2023.01.017.

References

[1] L.A. Bermúdez, J.M. Pascual, M.M. Martínez, J.M. Poyatos-Capilla, Effectiveness of advanced oxidation processes in wastewater treatment: state of the art, Water 13 (2021) 2094.
[2] W. Ismail, S. Mokhtar, Various methods for removal, treatment, and detection of emerging water contaminants, Emerg. Contam., Intechopen (2020) 27–38.
[3] P.E. Rosenfeld, L.G.H. Feng, Emerging Contaminants. Risks of Hazardous Wastes, William Andrew Publishing,, 2011, pp. 215–222.
[4] European Commission, Directorate-General for Environment, K. Kümmerer, Options for a Strategic Approach to Pharmaceuticals in the Environment: Final Report, 2019.
[5] M. Jureczko, J. Kalka, Cytostatic pharmaceuticals as water contaminants, Eur. J. Pharmacol. 866 (2020), 172816.
[6] E. Heath, M. Isidori, T. Kosjek, M. Filipic. Fate and Effects of Anticancer Drugs in the Environment, 1st ed..,, Springer, 2020.
[7] H. Franquet-Griell, C. Gómez-Canela, F. Ventura, S. Lacorte, Anticancer drugs: consumption trends in spain, prediction of environmental concentrations and potential risks, Environ. Pollut. 229 (2017) 505–515.
[8] M.H.F. Graumans, W.F.L.M. Hoeben, F.G.M. Russel, P.T.J. Scheepers, Oxidative degradation of cyclophosphamide using thermal plasma activation and UV/H_2O_2 treatment in tap water, Environ. Res. 182 (2020), 109046.
[9] L. Climent, Analysis of Chemotherapy Drugs and Related Compounds in Aquatic Environment: Removal, Transformation and Risk Evaluation in Eco-friendly and Advanced Technologies, Universitat de Girona, 2016.
[10] A.L. Garcia-Costa, A. Alves, L.M. Madeira, M.S.F. Santos, Oxidation processes for cytostatic drugs elimination in aqueous phase: a critical review, J. Environ. Chem. Eng. 9 (2021), 104709.
[11] D. Li, H. Chen, H. Liu, D. Schlenk, J. Mu, S. Lacorte, G.G. Ying, L. Xie, Anticancer drugs in the aquatic ecosystem: environmental occurrence, ecotoxicological effect and risk assessment, Environ. Int. 153 (2021), 106543.
[12] A. Tripathi, A. David, T. Govil, S. Rauniyar, N. Rathinam, K. Goh, R. Sani, Environmental Remediation of Antineoplastic Drugs: Present Status, Challenges and Future Directions, Processes, 8 (2020) 747.
[13] D. Ma, H. Yi, C. Lai, X. Liu, X. Huo, Z. An, L. Li, Y. Fu, B. Li, M. Zhang, L. Qin, S. Liu, L. Yang, Critical review of advanced oxidation processes in organic wastewater treatment, Chemosphere 275 (2021), 130104.
[14] N. Thomas, D.D. Dionysiou, S.C. Pillai, Heterogeneous fenton catalysts: a review of recent advances, J. Hazard. Mater. 404 (2021), 124082.
[15] M.H. Zhang, H. Dong, L. Zhao, D.X. Wang, D. Meng, A review on fenton process for organic wastewater treatment based on optimization perspective, Sci. Total Environ. 670 (2019) 110–121.
[16] M.M. Bello, A.A. Abdul-Raman, A. Asghar, A review on approaches for addressing the limitations of fenton oxidation for recalcitrant wastewater treatment, Process Saf. Environ. Prot. 126 (2019) 119–140.
[17] G.-X. Huang, C.-Y. Wang, C.-W. Yang, P.-C. Guo, H.-Q. Yu, Degradation of bisphenol A by peroxymonosulfate catalytically activated with Mn1.8Fe1.2O4 nanospheres: synergism between Mn and Fe, Environ. Sci. Technol. 51 (2017) 12611–12618.
[18] Y. Guan, G. Fu, Q. Wang, S. Ma, Y. Yang, B. Xin, J. Zhang, J. Wu, T. Yao, Fe, Co, N co-doped hollow carbon capsules as a full pH range catalyst for pollutant degradation via a non-radical path in Fenton-like reaction, Sep. Purif. Technol. 299 (2022), 121699.
[19] Council Directive 98/83/EC of 3 November 1998 on the quality of water intended for human consumption, Official Journal L 330, 1998, pp. 32–54.
[20] Y. Sun, P. Tian, D. Ding, Z. Yang, W. Wang, H. Xin, J. Xu, Y.F. Han, Revealing the active species of cu-based catalysts for heterogeneous fenton reaction, Appl. Catal. B: Environ. 258 (2019), 117985.
[21] S. Hussain, E. Aneggi, D. Goi, Catalytic activity of metals in heterogeneous fenton-like oxidation of wastewater contaminants: a review, Environ. Chem. Lett. 19 (2021) 2405–2424.
[22] Y. Bao, Q. Yan, J. Ji, B. Qiu, J. Zhang, M. Xing, Graphene-based photo-fenton catalysts for pollutant control, Trans. Tianjin Univ. 27 (2021) 110–126.
[23] X.J. Lee, B.Y.Z. Hiew, K.C. Lai, L.Y. Lee, S. Gan, S. Thangalazhy-Gopakumar, S. Rigby, Review on graphene and its derivatives: synthesis methods and potential industrial, Implement., J. Taiwan Inst. Chem. Eng. 98 (2019) 163–180.
[24] E.S. Emídio, P. Hammer, R.F.P. Nogueira, Simultaneous degradation of the anticancer drugs 5-fluorouracil and cyclophosphamide using a heterogeneous photo-Fenton process based on copper-containing magnetites ($Fe_{(3-x)}Cu_{(x)}O_{(4)}$), Chemosphere 241 (2020), 124990.
[25] C.A. Lutterbeck, L. Machado, È, K. Kümmerer, Photodegradation of the antineoplastic cyclophosphamide: a comparative study of the efficiencies of UV/H_2O_2, UV/Fe^{2+}/H_2O_2 and UV/TiO_2 Processes, Chemosphere 120 (2015) 538–546.
[26] J.C. Espinosa, S. Navalón, M. Álvaro, H. García, Reduc. Graph. Oxide a Met. -Free Catal. Light-Assist. Fenton- React. 8 (2016) 2642–2648.
[27] L.M. Pastrana-Martínez, S. Morales-Torres, V. Likodimos, J.L. Figueiredo, J. L. Faria, P. Falaras, A.M.T. Silva, Advanced nanostructured photocatalysts based on reduced graphene oxide-TiO_2 composites for degradation of diphenhydramine pharmaceutical and methyl orange dye, Appl. Catal., B 123–124 (2012) 241–256.
[28] J. Cencerrero, P. Sánchez, A. de Lucas-Consuegra, A.R. de la Osa, A. Romero, Influence of the reducing agent on the physicochemical and electrocatalytic properties of graphene-based aerogels, FlatChem 36 (2022), 100435.
[29] T.M. Eggenhuisen, H. Friedrich, F. Nudelman, J. Zečević, N.A.J.M. Sommerdijk, P. E. de Jongh, K.P. de Jong, Controlling the distribution of supported nanoparticles by aqueous synthesis, Chem. Mater. 25 (2013) 890–896.
[30] B.D. Cullity, S.R. Stock. Elements of X-ray Diffraction, Third edition.,, Prentice-Hall,, New York, 2001.
[31] S. Brunauer, P.H. Emmett, E. Teller, Adsorption of gases in multimolecular layers, J. Am. Chem. Soc. 60 (1938) 309–319.
[32] E.P. Barrett, L.G. Joyner, P.P. Halenda, The determination of pore volume and area distributions in porous substances. I. computations from nitrogen isotherms, J. Am. Chem. Soc. 73 (1951) 373–380.
[33] H. Hamad, E. Bailón-García, S. Morales-Torres, F. Carrasco-Marín, A.F. Pérez-Cadenas, F.J. Maldonado-Hódar, FunCtionalized Cellulose For The Controlled Synthesis Of Novel Carbon-ti Nanocomposites: Physicochemical And Photocatalytic Properties, Nanomaterials 10 (2020) 729.
[34] L.M. Pastrana-Martínez, N. Pereira, R. Lima, J.L. Faria, H.T. Gomes, A.M.T. Silva, DegradatIon Of Diphenhydramine By Photo-fenton Using Magnetically Recoverable Iron Oxide Nanoparticles As Catalyst, Chem. Eng. J. 261 (2015) 45–52.
[35] N. Sharma, V. Sharma, Y. Jain, M. Kumari, R. Gupta, S.K. Sharma, K. Sachdev, Synthesis and characterization of graphene oxide (GO) and reduced graphene oxide (rGO) for gas sensing application, Macromol. Symp. 376 (2017) 1700006.
[36] S.K. Lakhera, R. Venkataramana, A. Watts, M. Anpo, B. Neppolian, Facile Synthesis of Fe_2O_3/Cu_2O Nanocomposite and its Visible Light Photocatalytic Activity for the Degradation of Cationic Dyes, Res. Chem. Intermed. 43 (2017) 5091–5102.
[37] B.A. Aragaw, Reduced graphene oxide-intercalated graphene oxide nano-hybrid for enhanced photoelectrochemical water reduction, J. Nanostructure Chem. 10 (2020) 9–18.
[38] C. Nethravathi, M. Rajamathi, Chemically modified graphene sheets produced by the solvothermal reduction of colloidal dispersions of graphite oxide, Carbon 46 (2008) 1994–1998.
[39] J. Ederer, P. Janoš, P. Ecorchard, V. Štengl, Z. Bělčická, M. Šťastný, O. Pop-Georgievski, V. Dohnal, Quantitative determination of acidic groups in functionalized graphene by direct titration, React. Funct. Polym. 103 (2016) 44–53.
[40] L.M. Pastrana-Martínez, S. Morales-Torres, V. Likodimos, P. Falaras, J. L. Figueiredo, J.L. Faria, A.M.T. Silva, Role of oxygen functionalities on the synthesis of photocatalytically active graphene–TiO2 composites, Appl. Catal. B: Environ. 158–159 (2014) 329–340.
[41] S. Mustafa, S. Tasleem, A. Naeem, Surface charge properties of Fe_2O_3 in aqueous and alcoholic mixed solvents, J. Colloid Interf. Sci. 275 (2004) 523–529.
[42] S. Brunauer, L.S. Deming, W.E. Deming, E. Teller, On a theory of the van der waals adsorption of gases, J. Am. Chem. Soc. 62 (1940) 1723–1732.
[43] J.I. Paredes, S. Villar-Rodil, A. Martínez-Alonso, J.M.D. Tascón, Graphene oxide dispersions in organic solvents, Langmuir 24 (2008) 10560–10564.
[44] P. Solís-Fernández, R. Rozada, J.I. Paredes, S. Villar-Rodil, M.J. Fernández-Merino, L. Guardia, A. Martínez-Alonso, J.M.D. Tascón, Chemical and microscopic analysis of graphene prepared by different reduction degrees of graphene oxide, J. Alloy. Compd. 536 (Supplement 1) (2012) S532–S537.
[45] S. Biswas, A. Pal, T. Pal, Supported metal and metal oxide particles with proximity effect for catalysis, RSC Adv. 10 (2020) 35449–35472.
[46] Q. Xia, D. Zhang, Z. Yao, Z. Jiang, Revealing the enhancing mechanisms of Fe-Cu bimetallic catalysts for the fenton-like degradation of phenol, Chemosphere 289 (2021), 133195.
[47] H. Dan, Y. Kong, Q. Yue, J. Liu, X. Xu, W. Kong, Y. Gao, B. Gao, Magnetic field-enhanced radical intensity for accelerating norfloxacin degradation under FeCu/rGO photo-fenton catalysis, Chem. Eng. J. 420 (2021), 127634.
[48] P. Manickam-Periyaraman, J.C. Espinosa, B. Ferrer, S. Subramanian, M. Álvaro, H. García, S. Navalón, Bimetallic iron-copper oxide nanoparticles supported on nanometric diamond as efficient and stable sunlight-assisted photocatalyst, Chem. Eng. J. 393 (2020), 124770.
[49] G.H. Le, T.T. Nguyen, M.B. Nguyen, T.T.T. Quan, T.D. Nguyen, A. Sapi, I. Szenti, S. Mutyala, A. Kukovecz, Z. Konya, T.A. Vu, Cu–Fe incorporated graphene-oxide

nanocomposite as highly efficient catalyst in the degradation of dichlorodiphenyltrichloroethane (DDT) from aqueous solution, Top. Catal. 63 (2020) 1314–1324.